eNeuro

Research Article: Confirmation | Sensory and Motor Systems

Rapid Analysis of Visual Receptive Fields by Iterative Tomography

https://doi.org/10.1523/ENEURO.0046-21.2021

Cite as: eNeuro 2021; 10.1523/ENEURO.0046-21.2021

Received: 3 February 2021
Revised: 2 November 2021
Accepted: 12 November 2021

This Early Release article has been peer-reviewed and accepted, but has not been through the composition and copyediting processes. The final version may differ slightly in style or formatting and will contain links to any extended data.

Alerts: Sign up at www.eneuro.org/alerts to receive customized email alerts when the fully formatted version of this article is published.

Copyright © 2021 Eiber et al.

This is an open-access article distributed under the terms of the Creative Commons Attribution 4.0 International license, which permits unrestricted use, distribution and reproduction in any medium provided that the original work is properly attributed.

eNeuro Accepted Manuscript

eNeuro Accepted Manuscript

1 **Title:** Rapid analysis of visual receptive fields by iterative tomography

2 **Abbreviated title:** Receptive field analysis

3 **Authors and affiliations:** Calvin. D. Eiber[a,b,c], Jin Y. Huang[b], Spencer C. Chen[c], Natalie
4 Zeater[a,b,c], Alexander N. J. Pietersen[a,b,c], Dario. A. Protti[b], Paul. R. Martin[a,b,c]

5 [a] Save Sight Institute, The University of Sydney, Sydney, NSW 2000, Australia

6 [b] School of Medical Sciences, The University of Sydney, Sydney, NSW 2000, Australia

7 [c] Australian Research Council Centre of Excellence for Integrative Brain Function, The
8 University of Sydney, Sydney, NSW 2000, Australia

9 **Author contributions:** CDE JYH DAP and PRM designed research; all authors performed
10 research; CDE analyzed data; CDE and PRM wrote the paper.

11 **Correspondence**: P. R. Martin, email: paul.martin@sydney.edu.au, phone: +61 2 9382 7539,
12 Postal address: Save Sight Institute, 8 Macquarie St, Sydney 2001, Australia.

13 **Figures:** 6

14 **Tables:** 0

15 **Multimedia:** 0

16 **Number of words:** Abstract: 243/250, Significance statement 61/120; Introduction:
17 419/650; Discussion 767/1500

18 **Acknowledgements:** We thank A. Demir and R. Masri for technical assistance, and A. Wei
19 and H. Mansuri for assistance with mouse receptive field classification.

20 **Conflict of Interest:** Authors report no conflict of interest

21 **Funding sources:** Australian National Health & Medical Research Council Project grant
22 (1042609), Australian Research Council Centre of Excellence for Integrative Brain Function
23 (CE140100007), Australian Research Council grant (DP0988227).

24

eNeuro Accepted Manuscript

25 **ABSTRACT**

26 Many receptive fields in the early visual system show standard (center-surround) structure
27 and can be analyzed using simple drifting patterns and a Difference-of-Gaussian (DoG)
28 model, which treats the receptive field as a linear filter of the visual image. But many other
29 receptive fields show non-linear properties such as selectivity for direction of movement.
30 Such receptive fields are typically studied using discrete stimuli (moving or flashed bars and
31 edges) and are modelled according to the features of the visual image to which they are
32 most sensitive. Here, we harness recent advances in tomographic image analysis to
33 characterize rapidly and simultaneously both the linear and non-linear components of visual
34 receptive fields. Spiking and intracellular voltage potential responses to briefly flashed bars
35 are analyzed using non-negative matrix factorization (NNMF) and iterative reconstruction
36 tomography (IRT). The method yields high-resolution receptive field maps of individual
37 neurons and neuron ensembles in primate (marmoset, both sexes) lateral geniculate and
38 rodent (mouse, male) retina. We show that the first two IRT components correspond to
39 DoG-equivalent center and surround of standard (magnocellular and parvocellular)
40 receptive fields in primate geniculate. The first two IRT components also reveal the spatio-
41 temporal receptive field structure of non-standard (on/off-rectifying) receptive fields. In
42 rodent retina we combine NNMF-IRT with patch-clamp recording and dye injection to
43 directly map spatial receptive fields to the underlying anatomy of retinal output neurons.
44 We conclude that NNMF-IRT provides a rapid and flexible framework for study of receptive
45 fields in the early visual system.

46

47 **SIGNIFICANCE STATEMENT**

48 We present new means to characterize rapidly the linear and non-linear properties of
49 receptive fields in early stages of visual processing. We analyze light-evoked response
50 properties using new tomographic methods developed for medical imaging. The
51 tomographic method is rapid, can be used to characterize many cells simultaneously, and
52 reveals detailed structure of receptive field organization in monkey and mouse visual
53 system.

54

eNeuro Accepted Manuscript

eNeuro Accepted Manuscript

55 **INTRODUCTION**

56 Visual signal processing is the single largest activity of the human brain; by some estimates,
57 over half of primate neocortex receives visual signals (Felleman and Van Essen, 1991). But
58 what is the nature and purpose of these visual signals? Since the first descriptions of visual
59 receptive fields in single-neuron recordings from the eye of horseshoe crabs (Hartline,
60 1938), two main conceptual models for answering this question have been developed. One
61 model (Marr, 1982; Poggio et al., 1985) describes visual receptive fields as linear spatial
62 filters that send undifferentiated messages from the eye to the brain, where they can be
63 refined and analysed. The alternative model (Lettvin et al., 1959; Barlow, 1972) describes
64 receptive fields as non-linear feature detectors, which are selectively triggered by relevant
65 features in the visual environment and feed specific pathways for visually-guided behaviors.
66 Visual function depends however on the simultaneous integration of visual signals from
67 many cells, including cell types well-characterized by linear spatial filter models (Kuffler,
68 1953; Rodieck and Stone, 1965) as well as cells better described by trigger-feature models
69 (Hubel and Wiesel, 1961; Barlow and Levick, 1965; Riesenhuber and Poggio, 2002). This
70 practical (and, arguably, theoretical) inconsistency points to a need for methods which can
71 characterize linear– and non-linear receptive fields within the same framework.

72 Attempts to unify analyses of linear and non-linear receptive fields have included
73 methods based on responses to spatiotemporal noise, using the principle of reverse
74 correlation (De Boer and Kuyper, 1968; De Valois et al., 1979; Jones and Palmer, 1987;
75 Brown et al., 2000; Chichilnisky, 2001; Liu et al., 2017). The profound suppressive effects of
76 inhibitory circuits at the first stages of visual processing in the retina however largely restrict
77 such pseudo-random techniques to characterizing the linear kernel of visual responses.

eNeuro Accepted Manuscript

78 Further, there is a need for stimuli and analysis techniques which can robustly activate cell
79 ensembles comprising spatially distributed receptive fields. To accomplish these goals,
80 receptive field mapping using flashing bars and the inverse radon transform has been
81 demonstrated in the retina (Johnston et al., 2014; Stincic et al., 2016) and primary visual
82 cortex (Katona et al., 2012; Nauhaus et al., 2016). Here we advance these approaches by
83 articulating the radon transform with iterative reconstruction tomography (IRT) algorithms
84 adapted from the field of tomographic image analysis (Andersen and Kak, 1984; Hansen and
85 Jørgensen, 2018). The IRT method reveals detailed features of receptive field organization in
86 the pre-cortical visual system, and allows rapid analysis of linear and non-linear receptive
87 fields mapped for many cells simultaneously under a single experimental framework.

88 **Materials and Methods**

89 *Extracellular recordings*

90 Extracellular recordings were made from the lateral geniculate nucleus (LGN) of 6 adult
91 marmosets (*Callithrix jacchus,* 4 male, 2 female) using high-impedance single electrodes and
92 multielectrode arrays (NeuroNexus); 42 isolated single units included 11 parvocellular (P)
93 cells, 11 magnocellular (M) cells and 20 koniocellular (K) cells. Because K cells comprise
94 heterogenous sub-populations (reviewed by Hendry and Reid, 2000; Martin and Solomon,
95 2019), they were further classified according to their specific response properties. They
96 comprised 8 color-coding (blue/yellow-selective) K cells (Szmajda et al., 2006), 7 K-on/off
97 cells (Eiber et al., 2018b), and 5 K cells with other response properties. Procedures were
98 approved by the institutional animal care and ethics committee at the Author University.
99 Anesthesia and analgesia were maintained by continuous intravenous delivery of Sufentanil
100 citrate (6 – 30 μg kg^{-1} h^{-1}; Sufenta Forte, Janssen) and inspired 70:30 mix of N_2O and
101 carbogen. At the conclusion of the experiment, the animal was overdosed with

eNeuro Accepted Manuscript

102 pentobarbitone sodium (80–150 mg kg^{-1}, i.v.) and positions of recorded cells were
103 recovered histologically.

104 *Patch clamp recordings*

105 In-*vitro* whole-cell patch-clamp recordings of retinal ganglion cells (RGCs) were performed
106 in whole-mount retina from dark-adapted young adult male mice (C57Bl/6J, n = 15). Surgical
107 procedures in mice were carried out under low-light conditions using infrared or dim red
108 illumination. Animals were anesthetized by isoflurane (Pharmachem, AU), then euthanized
109 by cervical dislocation. Eyes were removed and the retina was dissected in carboxygenated
110 Ames medium (Sigma-Aldrich) and transferred to a recording chamber. During recording,
111 the recording bath was perfused with 36°C carboxygenated Ames medium. Whole-cell
112 patch-clamp recordings of RGCs took place under an Axioskop microscope (Zeiss) using
113 infrared light, with a K^+-gluconate-based intracellular solution containing Lucifer Yellow
114 (0.2%). At the end of each experiment retinae were fixed with 4% paraformaldehyde in 0.1
115 M phosphate buffer for 30 min then processed using anti-Lucifer Yellow antibodies
116 (1:10,000, Invitrogen) to reveal cell morphology. Most of the recorded cells (12/15) were
117 classified as type A (Sun et al., 2002; Bleckert et al., 2014), having large cell bodies with
118 radiating branching dendrites; the remainder were classified as type C6/J-RGC (3/15), having
119 an asymmetric comet-like dendritic field (Kim et al., 2008; Liu and Sanes, 2017). Cell
120 morphology was captured using a Leica SPE-II confocal microscope and images were
121 stitched and processed to align the traced dendritic morphology to the location of the cell
122 during recording using ImageJ, Adobe Photoshop and Illustrator. Dendritic fields were
123 traced in MATLAB using the maximum-intensity projections of the dendritic field images;
124 information regarding the stratification of the RGCs was discarded.

eNeuro Accepted Manuscript

125 *Visual stimulus*

126 Visual stimuli (flashing bars) were generated using custom visual stimulus software (EXPO,
127 Peter Lennie) at 6 different orientations and 21 positions per orientation, typically using 1 –
128 2 s presentations flashed at 5 Hz in the LGN and 1 – 2 Hz in the retina. For a subset of
129 marmoset LGN recordings, cone-selective stimuli were generated as described previously
130 (Brainard, 1996; Tailby et al., 2008) using the spectral radiance distribution of the monitor
131 phosphors, the spectral sensitivity of marmoset short-wave sensitive (S) and medium/long-
132 wave sensitive (ML) cone photoreceptors, and knowledge of the spectral absorbance of the
133 optic media and macular pigment (Tailby et al., 2008). Three replicates of this stimulus
134 procedure were presented; all stimuli were presented in pseudo-random order. In most
135 cases, there was no obvious difference between receptive field maps computed from a
136 single replicate compared to the analysis of all three replicates. In both mice and
137 marmosets, flashing bar recordings were complemented by more traditional recordings of
138 drifting grating responses to stimuli of varying contrast and spatial frequency, as well as
139 responses to flashed spots of various sizes. For retinal recordings, stimuli were presented at
140 intensity of 0.25 cd/m^2 on a dark background using a white OLED monitor (SVGA, 800 x 600
141 pixels, refresh rate: 60 Hz, eMagin Corp, white point CIE [x, y] [0.32, 0.33]). For LGN
142 recordings, stimuli were presented on a grey background (mean luminance 50 cd/m2) using
143 a LED monitor (VIEWPixx, Vpixx Technologies, refresh rate 120 Hz).

144 For cells recorded in the LGN, the contrast response function and temporal responses
145 to flashed spots were used to classify each recorded cell as either P, M, or a subclass of K
146 cell, as described in the results. For the majority of LGN cells (which lack significant S-cone
147 input), we found little difference between receptive fields mapped with achromatic stimuli
148 *vs* ML-cone-isolating stimuli. Receptive field analyses for these cells are based on

eNeuro Accepted Manuscript

149 achromatic stimuli if available, and ML-cone-isolating stimuli otherwise, as described below.
150 For purposes of statistical comparison, drifting grating responses in a reference population
151 of P cells (n = 130) and M cells (n = 90) were drawn from a larger database of recordings
152 conducted under similar recording conditions. To control for the influence of eccentricity on
153 the computed receptive field statistics, this dataset was reduced to an eccentricity-matched
154 set of 69 P cells and 69 M cells.

155 Results were mildly dependent on the choice of bar width and temporal frequency;
156 bar width and temporal frequency were set based on pilot experiments to give the best
157 compromise between response amplitude, data acquisition time (which is generally reduced
158 by broader bars) and spatial resolution (which is improved by narrower bars). For example,
159 we found that mapping RGC receptive fields with broader bars (90 *vs* 30 µm) and faster
160 stimuli (5 *vs* 1 Hz) tended to produce larger estimates of receptive field diameter. In a 3-way
161 ANOVA controlling for variation between cells (n = 74 stimulus sessions), increasing bar size
162 increased estimated diameter ($p = 0.001$) but the effect of temporal frequency was not
163 significant ($p = 0.072$). Where tested, changing spatial and temporal parameters did not
164 change the overall visual appearance of the receptive field map, nor the location of the
165 maximum response, nor the presence of transitions from positive to negative spatial
166 weights. The choice to stimulate using 6 orientations was made following Johnston et al.
167 (2014), who found that 5 orientations analyzed through filtered back-projection were
168 sufficient to estimate the center, size, shape and orientation of the receptive field center,
169 and that additional projections did not increase the amount of spatial information that
170 could be extracted. Under a reanalysis of our data including only 3 orientations we could
171 identify the receptive field center and basic organisation in 28/42 cells (66.67%). When

eNeuro Accepted Manuscript

172 three rather than six bars were used for reconstruction, star-shaped streak artifacts
173 (described further below) were more pronounced and we had difficulty reconstructing non-
174 gaussian receptive field structures such as annular or displaced binocular receptive fields.

175 *Response Analysis*

176 Extracellularly recorded action potentials were discriminated by on-line and off-line
177 principal component analysis (Expo; Blackrock offline spike sorter, Plexon); intracellular
178 recording action potentials were determined using simple threshold-crossing procedure.
179 Spike trains were analyzed offline using Matlab (R2015a, Mathworks, Natick MA). For each
180 cell, a maximally descriptive feature set of temporal profiles and spatial weights was
181 constructed from the individual trial spike responses using non-negative matrix factorization
182 (NNMF). The NNMF decomposition of the time-varying responses R to stimulus is given by

$$\boldsymbol{R}_{[i,t]} \cong \boldsymbol{P}_{[t,k]}\boldsymbol{W}_{[k,i]} \qquad \text{Eq. 1}$$

183 where $\boldsymbol{R}_{[i,t]}$ is a matrix of the individual response peristimulus time histograms (PSTHs),
184 containing the instantaneous spike-rate at time t as driven by the ith stimulus, which can be
185 represented as the product of a $t \times k$ matrix of up to k excitatory temporal profiles $\boldsymbol{P}_{[t,k]}$
186 and a $k \times i$ matrix of weights $\boldsymbol{W}_{[k,i]}$ representing the extent to which the response to the ith
187 stimulus matches profile $P_1 \dots P_k$. An example of this decomposition is shown in Fig. 1B-D,
188 which show the individual response PSTHs $\boldsymbol{R}_{[i,t]}$ (Fig. 1B), the computed weights $\boldsymbol{W}_{[k,i]}$ (Fig.
189 1C), and the temporal profiles $\boldsymbol{P}_{[t,k]}$ (Fig. 1D). The NNMF decomposition of the response
190 follows the same form as a principal component analysis where the primary differences P
191 and W are constrained to be non-negative. Responses to cone-isolating stimuli were
192 analyzed together to generate common temporal profiles, but distinct spatial weights for
193 the ith S-cone vs the ith ML-cone stimulus.

eNeuro Accepted Manuscript

194 Due to the non-negativity constraints on the temporal profiles, the approach outlined
195 above only captures excitatory components of the receptive field structure. In order to
196 recover the inhibitory components of the center and surround, the non-negativity
197 constraint on the temporal component of the wave profiles was relaxed according to

$$\boldsymbol{R}_{[i,t]} \cong \boldsymbol{P}_{[t,k]}\boldsymbol{W}_{[\boldsymbol{k},\boldsymbol{i}_s]} = (\boldsymbol{P}\,\boldsymbol{F}^{-1})(\boldsymbol{F}\,\boldsymbol{W}) \qquad \text{Eq. 2}$$

198 where the rotation matrix $\boldsymbol{F}$ (dimension k_{max}) has entries of 1 on the diagonal and
199 nonnegative values elsewhere. Equation (2) allows for negative values in the rotated
200 response components $(\boldsymbol{P}\,\boldsymbol{F}^{-1})$, while preserving the rotated NNMF component weights
201 $(\boldsymbol{F}\,\boldsymbol{W})$ as positive values. In order to generate approximately unimodal (spatially compact)
202 spatial weights, response weights were rotated to fit Gaussian profiles as given by

$$(\boldsymbol{FW})_k = g_k\, e^{-\left(\frac{d_i}{4\,r_k}\right)^2} + b_k \qquad \text{Eq. 3}$$

203 Where the kth rotated response weight $(\boldsymbol{FW})_k$ is a scaled Gaussian function of distance
204 from the receptive field centre with height g_k . The distance from the ith stimulus to the
205 receptive field center is d_i, the radius of the nth component is r_n, and the baseline
206 activation of the nth component is b_n. For a simple 2-component centre-surround response,
207 this model has 10 free parameters: 2 for the off-diagonal entries of F, 2 for the receptive
208 field center coordinate, and a radius, amplitude, and baseline level for each component.
209 Optimum values of parameters $\boldsymbol{W}$ and $\boldsymbol{F}$ in equation (3) were estimated in MATLAB using
210 constrained non-linear least-squares minimization with the off-diagonal entries of $\boldsymbol{F}$ (Eq. 3)
211 initialized to 0. Equation (3) provides a parametric estimate of the receptive field diameter,
212 which was adjusted to account for the finite bar-width of the flashing-bar stimulus, and can
213 be compared to traditional measurements of receptive field diameter using drifting gratings

eNeuro Accepted Manuscript

214 at different spatial frequencies. Example data and MATLAB scripts implementing the NNMF-
215 IRT analysis and receptive field visualization are available at
216 https://github.sydney.edu.au/ceiber/rapid-RF-analysis

217 *Selection of number of NNMF components*

218 In order to determine the number of NNMF components to analyze, temporal profiles and
219 mapped spatial weights were visualized for a range of choices of k_{max}. The number of
220 components was increased until either 1) additional components generated temporal
221 profiles which did not change from pre-stimulus to stimulus on visual inspection, or 2)
222 additional components primarily separated responses to stimuli of different orientations, as
223 opposed to response components with distinct temporal profiles. When responses were
224 over-segmented in this way, the NNMF analysis produced inconsistent sinograms which
225 could not be spatially reconstructed. For consistency, all data was analyzed with $k_{max} \geq 2$.

226 *Receptive field reconstruction*

227 The inverse radon transform is a general inverse problem, where a solution to the linear
228 system $\boldsymbol{y} = \boldsymbol{A}\,\boldsymbol{x}$ is sought. The measured data $\boldsymbol{y} = [y_1 \dots y_s]^{\mathrm{T}}$ are the average component
229 weights from equation (1) or (2) for each stimulus $1 \dots s$, which are given by the matrix
230 product of $\boldsymbol{A}$, an $s \times p$ matrix of the stimulus where each row is the image corresponding to
231 the ith stimulus, and $\boldsymbol{x}$, a $p \times 1$ vector of the point-wise strength of the receptive field at
232 each point in visual space. This problem is ill-posed when the dimension of the receptive
233 field map (number of pixels p) is greater than the number of measurements s. This problem
234 can be solved with the simultaneous algebraic reconstruction technique (SART) (Andersen
235 and Kak, 1984; Hansen and Jørgensen, 2018), using the normalized cumulative periodogram
236 stopping rule (Hansen et al., 2006; Rust and O'Leary, 2008). For comparison, filtered back-
237 projections were computed for the receptive field component weights using a first-order

eNeuro Accepted Manuscript

238 low-pass Butterworth filter with a normalized corner frequency of 0.8 cycles following
239 reference (Johnston et al., 2014). The SART algorithm is one of a family of fast simultaneous
240 iterative reconstruction algorithms; comparison showed negligible difference in
241 reconstruction performance between SART and other similar algorithms (Hansen and
242 Jørgensen, 2018) (data not shown). For chromatic stimuli, receptive fields were computed
243 from the spatial weights of the S-cone- and ML-cone-isolating stimuli independently.

244 *Experimental design and statistics*

245 Receptive field parameters estimated from the NNMF-IRT Gaussian fits given by equation
246 (3) were compared with estimates based on responses to drifting gratings of varying spatial
247 frequency. The standard difference-of-Gaussians (DoG) model (Rodieck and Stone, 1965;
248 Enroth-Cugell and Robson, 1966) was used to analyze the first harmonic (f1) response of the
249 drifting grating response:

$$K = \pi k_c r_c^2 e^{-(\pi r_c \omega)^2} - \pi k_s r_s^2 e^{-(\pi r_s \omega)^2} \qquad \text{Eq. 4}$$

250 where the response spike rate K is a function of the strength of the center and surround
251 (given by k_c and k_s) and the radius of the center and surround (given by r_c and r_s), for an
252 input stimulus ω (in cycles/degree). The ratio of surround to center gain (fig. 4B) is k_s/k_c.
253 For purposes of comparison, first harmonic (f1) responses were estimated from the NNMF
254 component profiles in LGN cells; a comparison of the fitted parameters for drifting grating
255 and flashing bar stimuli for P and M cells is shown in the results, Fig. 5. All comparison
256 statistics are based on two-sided Wilcoxon rank sum tests for independent samples (unless
257 otherwise stated), and are corrected for multiple comparisons using the Holm-Bonferroni
258 method.

eNeuro Accepted Manuscript

259

260 **RESULTS**

261 *Matrix factorization of flashing bar responses*

262 Responses were collected *in vivo* from extracellular recordings of single units in the LGN of
263 marmosets (*Callithrix jacchus*, n = 6 animals); 42 isolated single units included 11
264 parvocellular (P) cells, 11 magnocellular (M) cells and 20 koniocellular (K) cells. Responses
265 were also collected *in vitro* in patch-clamp recordings from whole-mount retina of dark-
266 adapted mice (n = 15 cells in 15 animals). The visual stimuli were stationary flashing (square-
267 wave modulated) bars, presented at 5 Hz in the LGN and 1–2 Hz in the retina, for 1-2 s per
268 stimulus. The stimulus set comprised bars at 6 different orientations and 21 positions per
269 orientation. Using three replicates of this set of stimuli presented in pseudo-random order,
270 complete receptive field maps could be collected for single-cell or array recordings in under
271 5 minutes per replicate. Fig. 1B shows sample responses to three replicates of achromatic
272 flashing bar stimuli for a typical LGN M-on cell.

273 Peri-stimulus time histograms (PSTHs, Fig. 1B) were constructed for each replicated
274 trial. Non-negative matrix factorization (NNMF) was applied to decompose the spike-rate
275 into temporal profiles (Fig. 1D) and corresponding spatial weights (Fig. 1C). These spatial
276 weights were mapped to form a receptive field image using iterative reconstruction
277 tomography (IRT, Fig. 1E). Previous work which used white-noise stimuli and a similar
278 reconstruction approach required 60-180 minutes recording time (Liu et al., 2017). In
279 common with principal component analysis (Schwartz et al., 2006), NNMF yields a low-
280 dimensional representation of the response as a sum of k independent components (see
281 'Selection of number of NNMF components', methods). Unlike principal component
282 analysis, the non-negativity constraints mean that NNMF yields a sparse representation of

eNeuro Accepted Manuscript

283 independent response elements (Ding et al., 2005), and is mildly tolerant of non-
284 stationarities in the recorded data. We limited analyses to decompositions of two or three
285 components, as demonstrated in Fig. 1C-E. Structure could sometimes be observed in
286 mapped spatial weights corresponding to additional components, but these were not
287 systemically investigated further. In common with previous approaches (Johnston et al.,
288 2014) receptive field maps for the first two NNMF components generated using IRT show
289 weak "streak" artefacts; the origin and impact of these artefacts is discussed further below.

290 The M-on cell receptive field center mechanism dominates the first NNMF component,
291 appearing as a phase-locked response in the component PSTH (Fig. 1D upper) and as a small
292 roughly circular region on the IRT weights map (Fig. 1E upper). The second component PSTH
293 comes in opposite phase to the first component, (Fig. 1D center) and appears as an annular
294 region in the IRT weight map (Fig. 1E center). The second NNMF component thus shows the
295 excitatory contribution of the surround to spiking responses. The third NNMF component
296 comes in phase with the surround (Fig. 1D lower) within a spatially broad region (Fig. 1E
297 lower) which likely corresponds to the extra-classical suppressive field (Solomon et al.,
298 2002). These data show that the NNMF-IRT analysis can cleanly separate well-characterized
299 components of concentric antagonistic receptive fields in marmoset LGN.

300 *Simultaneous receptive field mapping.*

301 We next show that the NNMF-IRT procedure can be used to map receptive fields from cells
302 recorded simultaneously through semiconductor array electrodes. Figure 2A shows the
303 reconstructed positions of five LGN cells (one P-on cell, two K-on/off cells, and two K blue-
304 on cells) in response to cone-isolating stimuli. Half-maximal and 90% sensitivity contours for
305 first NNMF components of these cells (Fig. 2B) show expected visuotopic progression and

eNeuro Accepted Manuscript

306 receptive field dimensions (White et al., 1998). Responses of the P-on cell (Fig. 2C,D upper)
307 are dominated by the excitatory contribution of the receptive field center. The K-on/off cell
308 (Fig. 2C,D center) received weak excitatory binocular input from the non-dominant eye,
309 resulting in a displaced hot-spot in the receptive field map (arrowhead, Fig. 2D). This
310 observation is consistent with our previous report of binocular inputs to K cells (Zeater et
311 al., 2015). The K blue-on cells (Fig. 2C,D lower) showed opposite-sign responses to S-cone
312 isolating and ML-cone isolating stimuli. These response patterns are consistent with
313 responses to drifting, cone-isolating gratings in single-cell recordings (Eiber et al., 2018). The
314 results show the NNMF-IRT analysis can map the spatio-temporal and chromatic inputs to
315 simultaneously recorded linear and non-linear receptive fields, with data acquisition time a
316 fraction that required for traditional grating-based analyses. Importantly, responses to
317 individual stimuli were not strongly suppressed by non-specific activation of suppressive
318 surround mechanisms, which is a chief limitation of approaches where much of the visual
319 field is activated simultaneously (as in, for example, full-field stimulation or pseudorandom
320 checkerboard stimulation).

321 *Quantitative analysis of spatiotemporal receptive fields*

322 The NNMF approach can be extended to visualize inhibitory receptive field components, as
323 opposed to sums of purely excitatory components. When we transformed the generated
324 spatial weights to best approximate unimodal Gaussian curves (see Methods, eq. 2), the
325 corresponding *temporal* response profiles had negative values, representing inhibitory
326 inputs to the receptive field (Fig. 3A: the reader should note that this example cell is not the
327 same cell as shown in Fig. 2C). In this way, the NNMF approach can be used to bridge
328 between different perspectives regarding receptive field organization. Receptive field radii
329 were computed from the resulting (Gaussian) rotated weights (Fig. 3C), and these weights

eNeuro Accepted Manuscript

330 can be mapped using IRT to show the resulting receptive field structure (Fig. 3D). For linear
331 LGN cells, this recombination yields the expected center and surround components
332 (example P cell, Fig. 3 upper; example M cell, Fig. 3 center). The surround profile is
333 substantially more prominent for M cells than for P cells, likely in consequence of the
334 characteristic high contrast gain of M cells (Derrington and Lennie, 1984; Kaplan and
335 Shapley, 1986). For M cells (but not P cells) we also observed bar positions that gave
336 frequency-doubled responses (data not shown) similar to those evoked by flickering
337 counter-phase gratings (Crook et al., 2008).

338 In addition to characterizing linear receptive fields, the NNMF-IRT analysis can probe
339 receptive fields of highly non-linear cells. For example, on applying NNMF-IRT to responses
340 of a K-on/off cell, the first NNMF component captures a rapidly adapting component which
341 responded preferentially to the first bar presentation (Fig. 3B lower). The second
342 component captured a non-adapting component which responded equally well across all
343 stimulus presentations in the 2 s period. Both components show evidence of frequency-
344 doubling. For this cell, the two components map as overlapping excitatory input fields (Fig.
345 3C, D lower). As expected (Eiber et al., 2018), the overall extent of the receptive field for this
346 K-on/off cell is broader than that of either the P or M cell receptive field center.

347 Observed differences between P cells and M cells are supported by population
348 statistics (Fig. 4). Measured using flashing bars, P cells had a mean receptive field center
349 radius of 0.04° ± 0.02 (N = 11) and our population of M cells had a larger mean receptive
350 field center radius of 0.12° ± 0.06 (N = 11, $p < 0.001$). Recorded P cells have a significantly
351 lower ratio of surround to center gain, compared to M cells (Fig. 4A, $p < 0.001$; population
352 mean ± SD for P cells 0.24 ± 0.15 imp s^{-1} vs 0.75 ± 0.40 for M cells). These data are

eNeuro Accepted Manuscript

353 quantitatively comparable to data obtained using drifting gratings in a large eccentricity-
354 matched sample of P and M cells (Fig. 4B). For K blue-on and K blue-off cells, the relative
355 gain of S-cone to ML-cone inputs was tightly correlated ($r = 0.94$, $p = 0.002$, $n=7$), with a
356 population mean ratio of 1.17 ± 0.61. Estimated NNMF-IRT spatial properties were likewise
357 correlated with counterpart parameters measured in the same cells using drifting gratings
358 (Fig. 4C); for example, center radii derived from NNMF-IRT and gratings were closely
359 correlated, $r = 0.84$ ($p < 0.001$). Receptive field radii could also be calculated using NNMF-IRF
360 for a small number of highly non-linear K-on/off cells ($n=3$, Fig. 4A,C). In sum, these data
361 show that NNMF-IRT yields estimates of spatial receptive field properties with accuracy at
362 least as high as measured using traditional grating stimuli. Further, data aquisition time
363 under the NNMF-IRT method (under five minutes per replicate, see methods) is much more
364 rapid than under traditional grating stimuli. For example, the spatial– and orientation tuning
365 measurements summarized in Figure 4 required acquisition times greater than 40 minutes
366 per cell for drifting grating stimuli. This time benefit is further increased by the capacity of
367 NNMF-IRT to characterize simultaneously cells with spatially separated receptive fields (as
368 shown by the example recording in Fig. 2).

369 *Comparison to underlying anatomy*

370 Directly correlating neural structure to neural function is important for improved
371 understanding the origins of visual receptive fields. We therefore compared receptive fields
372 mapped with NNMF-IRT to the underlying anatomy of RGCs in mouse retina, as previously
373 demonstrated by Brown et al. (2000) using spatiotemporal white noise. Example
374 intracellular recordings of flash bar responses for three retinal ganglion cells (RGCs, Fig. 5A)
375 are shown together with reconstructed dendritic morphologies (Fig. 5B), shown at the same
376 scale as the spatial weight map of the first NNMF-IRT component (Fig. 5C). In common with

eNeuro Accepted Manuscript

377 the linear P and M cells we recorded in marmoset LGN (Figs. 1,2,3), the first NNMF-IRF
378 component captures the linear center mechanism of the A-type receptive fields (Fig. 5,
379 upper rows). In contrast, the class C6/J-RGC cell response (Fig. 5A, lower) shows substantial
380 non-linearity. Here, the first three NNMF components capture excitatory responses with
381 distinct latency differences. The weight maps of the first three components are spatially
382 offset, in the same progression as the latency offsets (Fig. 5B lower). This example is
383 consistent with the known selectivity of C6/J-RGC cells for downward retinal image slip (Kim
384 et al., 2008; Liu and Sanes, 2017), but a more extensive study of direction selectivity is
385 beyond the scope of the present study. Across recorded cells, the anatomically measured
386 dendritic field correlated closely with the diameter of the physiological receptive field
387 extracted from the first NNMF-IRT component. (Fig. 5D, $r = 0.621$, $p = 0.018$).

388 The local structure of the NNMF-IRF spatial weight map (Fig. 6A) showed mild to
389 strong correlation with the local dendritic field density of recorded retinal ganglion cells (Fig.
390 6B, C), after accounting for the lateral spread of signal (estimated half-height radius 54.7
391 µm) induced by the presynaptic bipolar and amacrine cell circuitry. Across recorded cells the
392 mean r^2 correlation of anatomical to physiological measures was 0.543 ± 0.256 (Fig. 6D). In
393 sum, these results show the potential of NNMF-IRT analysis for fine-grained analysis of
394 structure-function relationships.

395 **DISCUSSION**

396 Here, we build on receptive field mapping techniques using to flashing bar stimuli (Johnston
397 et al., 2014) by combining non-negative matrix factorization (NNMF) with iterative
398 reconstruction tomography (IRT). This NNMF-IRT combination allows simultaneous
399 evaluation of linear and non-linear receptive fields, such as those of direction-selective C6/J-

400 RGCs (Fig. 5) and koniocellular on/off LGN cells (Fig. 3), and can be applied to characterize
401 many receptive fields in parallel. Because each location in the stimulus field is probed
402 independently by a high-contrast bar, the spatial and temporal contributions of weak
403 presynaptic inputs to receptive field can be measured (Fig. 6). The IRT method (Andersen
404 and Kak, 1984) preserves the spatial structure of such weak inputs while reducing the
405 influence of measurement noise, and permits incorporation of prior knowledge into the
406 receptive field reconstruction process (as shown in Fig. 3).

407 The fine structure of RGC receptive fields is driven by branching patterns of RGC
408 dendrites in the inner plexiform layer of the retina (Brown et al., 2000), with branch density
409 manifest as subunits in the computed receptive field (cf. Brown et al., 2000; Turner et al.,
410 2018; Eiber et al., 2018). The NNMF-IRT method offers a way forward for mapping receptive
411 field subunits, because the spatial resolution of the flashing bar maps can be increased
412 independently of bar contrast. The correspondence of receptive fields mapped using the
413 NNMF-IRT method with receptive fields mapped using complementary techniques such as
414 reverse correlation of spatiotemporal noise (De Boer and Kuyper, 1968; De Valois et al.,
415 1979; Jones and Palmer, 1987; Brown et al., 2000; Chichilnisky, 2001; Liu et al., 2017) will be
416 important to substantiate or refute the utility of the NNMF-IRT method.

417 A well-established advantage of NNMF for analyzing non-negative inputs such as
418 spike rates is the ease with which the resulting components can be interpreted. The non-
419 negativity constraint acts to bring correlated responses together by increasing the sparsity
420 (fraction of zero or near-zero weights) of the receptive field representation. Subunit-based
421 analyses (e. g. Turner et al., 2018; Liu et al., 2017) share this advantage, and both
422 approaches stand in contrast to a strict orthogonal basis vector representation, as would be

eNeuro Accepted Manuscript

eNeuro Accepted Manuscript

423 generated by singular value decomposition (SVD). The effect on the NNMF-derived
424 receptive field maps of response correlations arising from activation of multiple subunits is
425 however not yet known, and requires more research.

426 We found that NNMF usually led to two or three (very rarely, four) components
427 which could be interpreted in terms of both the temporal response profile (showing a
428 distinct response to stimulation) and the spatial response map (showing a clear center or
429 center-surround structure). We also tested SVD as a tool for response decomposition but
430 found that SVD rarely led to more than a single interpretable response component (data not
431 shown). When higher-order SVD components had a coherent spatial structure, they had an
432 unintelligible temporal structure, and vice-versa. We predict that additional NNMF
433 components will be useful for analyzing receptive field subunit structure at spatial
434 resolution greater than that presented here (e.g. Turner et al., 2018).

435 One limitation that IRT shares with the filtered back projection method is the presence
436 of star-shaped streak artefacts in the receptive field map (Johnston et al., 2014). Our pilot
437 reconstructions of synthetic receptive fields (data not shown) indicate that streak artifacts
438 can be reduced by measuring at more orientations, albeit at the cost of increased
439 acquisition time. Minimizing such receptive field artifacts is particularly important for
440 characterizing non-linear receptive fields such as those in smooth monostratified RGCs in
441 primates (Rhoades et al., 2019) and loom-detecting RGCs in mouse retina (Katz et al., 2016).
442 Another limitation of our present NNMF-IRT analysis approach was that we were unable to
443 disentangle the excitatory and inhibitory/suppressive components of the receptive field
444 surround in a model-agnostic manner; future work will concentrate on finding better ways
445 to separate these physiologically distinct mechanisms.

446 We conclude that the NNMF-IRT combination offers a flexible method to isolate
447 receptive field inputs for both linear and non-linear visually responding cells. As with the
448 filtered back-projection method, the mapping procedure is very rapid – accurate receptive
449 field maps can be constructed from as little as 5 minutes of data acquisition. This efficiency
450 offers the possibility to measure receptive fields before and after pharmacological
451 manipulations, and to explore contributions of local synaptic processing to receptive field
452 properties in vision. The combination of NNMF and IRT provides a new tool for studying
453 retinogeniculate projections and synaptic signal transformations underlying visual receptive
454 field organization. More broadly, the combination of NNMF and IRT offers an avenue to
455 unify linear (systems-theory) and non-linear (feature-detector) descriptions of cells in the
456 early visual system.

eNeuro Accepted Manuscript

eNeuro Accepted Manuscript

457 **References**

458 Andersen AH, Kak AC (1984) Simultaneous algebraic reconstruction technique (SART): a
459 superior implementation of the ART algorithm. Ultrasonic Imag 6:81-94.
460 Barlow HB, Levick WR (1965) The mechanism of directionally selective units in rabbit's
461 retina. J Physiol 178:477-504.
462 Barlow HB (1972) Single units and sensation: a neuron doctrine for perceptual psychology.
463 Neuron 1:371-394.
464 Bleckert A, Schwartz GW, Turner MH, Rieke F, Wong RO (2014) Visual space is represented
465 by nonmatching topographies of distinct mouse retinal ganglion cell types. Curr Biol
466 24:310-315.
467 Brainard DH (1996) Cone contrast and opponent modulation color spaces. In: Human Color
468 Vision (Kaiser PK, Boynton GM, eds), pp. 563-577. Washington, D. C.: Optical Society of
469 America.
470 Brown SP, He S, Masland RH (2000) Receptive field microstructure and dendritic geometry
471 of retinal ganglion cells. Neuron 27:371-383.
472 Chichilnisky EJ (2001) A simple white noise analysis of neuronal light responses. Network
473 12:199-213.
474 Crook JD, Peterson BB, Packer OS, Robinson FR, Troy JB, Dacey DM (2008) Y-cell receptive
475 field and collicular projection of parasol ganglion cells in macaque monkey retina. J
476 Neurosci 28:11277-11291.
477 De Boer E, Kuyper P (1968) Triggered correlation. IEEE Trans Biomed Eng 169-179.
478 De Valois KK, De Valois RL, Yund EW (1979) Responses of striate cortex cells to grating and
479 checkerboard patterns. Curr Biol 291:483-505.

eNeuro Accepted Manuscript

480 Derrington AM, Lennie P (1984) Spatial and temporal contrast sensitivities of neurones in
481 lateral geniculate nucleus of macaque. J Neurophysiol 357:219-240.
482 Ding C, He X, Simon HD (2005) On the equivalence of nonnegative matrix factorization and
483 spectral clustering. J Neurophysiol 606-610.
484 Eiber CD, Rahman AS, Pietersen ANJ, Zeater N, Dreher B, Solomon SG, Martin PR (2018)
485 Receptive Field Properties of Koniocellular On/Off Neurons in the Lateral Geniculate
486 Nucleus of Marmoset Monkeys. J Neurosci 38:10384-10398.
487 Enroth-Cugell C, Robson J (1966) The contrast sensitivity of retinal ganglion cells of the cat. J
488 Neurophysiol 187:517-552.
489 Felleman DJ, Van Essen DC (1991) Distributed hierarchical processing in the primate cerebral
490 cortex. Cereb Cortex 1:1-47.
491 Hansen PC, Jørgensen JS (2018) AIR Tools II: algebraic iterative reconstruction methods,
492 improved implementation. Numer Algor 79:107-137.
493 Hansen PC, Kilmer ME, Kjeldsen RH (2006) Exploiting residual information in the parameter
494 choice for discrete ill-posed problems. Numer Algor 46:41-59.
495 Hartline HK (1938) The response of single optic nerve fibres of the vertebrate eye to
496 illumination of the retina. Am J Physiol 121:400-415.
497 Hubel DH, Wiesel TN (1961) Integrative action in the cat’s lateral geniculate body. J
498 Neurophysiol 155:385-398.
499 Johnston J, Ding H, Seibel SH, Esposti F, Lagnado L (2014) Rapid mapping of visual receptive
500 fields by filtered back projection: application to multi-neuronal electrophysiology and
501 imaging. J Neurophysiol 592:4839-4854.
502 Jones JP, Palmer LA (1987) An evaluation of the two-dimensional gabor filter model of
503 simple receptive fields in cat striate cortex. J Neurophysiol 58:1233-1258.

eNeuro Accepted Manuscript

504 Kaplan E, Shapley RM (1986) The primate retina contains two types of ganglion cells, with
505 high and low contrast sensitivity. Proc Natl Acad Sci USA 83:2755-2757.
506 Katona G, Szalay G, Maák P, Kaszás A, Veress M, Hillier D, Chiovini B, Vizi ES, Roska B, Rózsa
507 B (2012) Fast two-photon in vivo imaging with three-dimensional random-access
508 scanning in large tissue volumes. Nature 9:201-208.
509 Katz ML, Viney TJ, Nikolic K (2016) Receptive field vectors of genetically-identified retinal
510 ganglion cells reveal cell-type-dependent visual functions. Nat Rev Neurosci
511 11:e0147738.
512 Kim IJ, Zhang Y, Yamagata M, Meister M, Sanes JR (2008) Molecular identification of a
513 retinal cell type that responds to upward motion. Nature 452:478-482.
514 Kuffler SW (1953) Discharge patterns and functional organization of mammalian retina. J
515 Neurophysiol 16:37-68.
516 Lettvin JY, Maturana HR, McCulloch WS, Pitts WS (1959) What the frog's eye tells the frog's
517 brain. Proc Inst Radio Engrs 47:1940-1951.
518 Liu J, Sanes JR (2017) Cellular and molecular analysis of dendritic morphogenesis in a retinal
519 cell type that senses color contrast and ventral motion. J Neurosci 37:12247-12262.
520 Liu JK, Schreyer HM, Onken A, Rozenblit F, Khani MH, Krishnamoorthy V, Panzeri S, Gollisch
521 T (2017) Inference of neuronal functional circuitry with spike-triggered non-negative
522 matrix factorization. Nat Commun 8:149.
523 Marr D (1982) Vision: a computational investigation in the human representation and
524 processing of visual information. New York: W. H. Freeman.
525 Nauhaus I, Nielsen KJ, Callaway EM (2016) Efficient receptive field tiling in primate V1.
526 Neuron 91:893-904.

eNeuro Accepted Manuscript

527 Poggio T, Torre V, Koch C (1985) Computational vision and regularization theory. Nature
528 317:314-319.
529 Rhoades CE, Shah NP, Manookin MB, Brackbill N, Kling A, Goetz G, Sher A, Litke AM,
530 Chichilnisky EJ (2019) Unusual physiological properties of smooth monostratified
531 ganglion cell types in primate retina. Neuron 103:658-672. e6.
532 Riesenhuber M, Poggio T (2002) Neural mechanisms of object recognition. Curr Opin
533 Neurobiol 12:162-168.
534 Rodieck RW, Stone J (1965) Analysis of receptive fields of cat retinal ganglion cells. J
535 Neurophysiol 28:833-849.
536 Rust BW, O'Leary DP (2008) Residual periodograms for choosing regularization parameters
537 for ill-posed problems. Numer Algor 24:034005.
538 Schwartz O, Pillow JW, Rust NC, Simoncelli EP (2006) Spike-triggered neural
539 characterization. Nature 6:484-507.
540 Solomon SG, White AJR, Martin PR (2002) Extraclassical receptive field properties of
541 parvocellular, magnocellular and koniocellular cells in the primate lateral geniculate
542 nucleus. J Neurosci 22:338-349.
543 Stincic T, Smith RG, Taylor WR (2016) Time course of EPSCs in ON-type starburst amacrine
544 cells is independent of dendritic location. Proc Natl Acad Sci USA 594:5685-5694.
545 Sun W, Li N, He S (2002) Large-scale morphological survey of mouse retinal ganglion cells. J
546 Comp Neurol 451:115-126.
547 Tailby C, Szmajda BA, Buzás P, Lee BB, Martin PR (2008) Transmission of blue (S) cone signals
548 through the primate lateral geniculate nucleus. Cereb Cortex 586:5947-5967.

eNeuro Accepted Manuscript

549 Turner MH, Schwartz GW, Rieke F (2018) Receptive field center-surround interactions
550 mediate context-dependent spatial contrast encoding in the retina. Nat Rev Neurosci
551 7:e38841.
552 White AJR, Goodchild AK, Wilder HD, Sefton AE, Martin PR (1998) Segregation of receptive
553 field properties in the lateral geniculate nucleus of a New-World monkey, the
554 marmoset Callithrix jacchus. J Neurophysiol 80:2063-2076.
555 Zeater N, Cheong SK, Solomon SG, Dreher B, Martin PR (2015) Binocular visual responses in
556 primate lateral geniculate nucleus. Curr Biol 25:3190-3195.
557

558

559

eNeuro Accepted Manuscript

560 **Figure Legends**

561

562 **Figure 1.** Schematic example of tomographic analysis. **A:** Example stimulus locations
563 (achromatic flashing bar, 5 Hz) presented to a magnocellular M-on cell (10.3° eccentricity) in
564 marmoset LGN. **B:** Raster of spike responses (1 row / trial) and peri-stimulus histograms
565 (PSTHs) to 2 s of stimulation at 5 Hz. Horizontal bar shows stimulus onset and duration. **C:**
566 Computed NNMF weights for each bar position, normalized to 100% per-weight maximum,
567 corresponding to the PSTHs shown in (B). **D:** Response component profiles from NNMF
568 analysis, corresponding to center and surround mechanisms. In order to emphasize the non-
569 negativity of the NNMF output, pre-stimulus baselines were not subtracted from the
570 components displayed. **E:** Receptive field maps of the component weights shown in (C).
571 Negative values indicate inhibitory contributions to the spatial summation for that
572 component.

573

574 **Figure 2.** Geniculate array recording. **A:** Reconstructed LGN and electrode track, showing
575 the location of 16 channels relative to the layers of the LGN. Two K blue-on cells, two K-
576 on/off cells, and one P-on cell were recorded from this site. **B:** Contour plot of
577 simultaneously recorded RFs for these cells to cone-isolating stimuli, showing outlines at
578 90% and 50% of the peak response amplitude (filled / shaded areas). **C:** NNMF component
579 profiles for three example cells; pre-stimulus baselines were not subtracted. Horizontal bar:
580 stimulus onset and duration. **D:** Receptive field maps corresponding to the components
581 shown in C. For the K-on/off cell a displaced hot-spot (attributable to weak excitatory input
582 from the non-dominant eye) is indicated with an open arrowhead. For the K blue-on cell,
583 spatially coextensive inputs are evident for S-cone-isolating and ML-cone-isolating stimuli.

eNeuro Accepted Manuscript

584

585 **Figure 3.** Analysis of geniculate receptive field structure. **A:** NNMF component profiles for
586 three example cells recorded in marmoset LGN in response to achromatic flashed bars.
587 Upper–lower: P-on cell, M-on cell, K-on/off cell (respective eccentricity 1.6°, 14.6°, and
588 29.2°). Each row shows one example cell. Sine waves show the response at the stimulus
589 frequency (5 Hz for the P and M cell; 10 Hz for the K-on/off cell). For the P and M cell, the
590 two components capture the responses of the center and the surround; for the K-on/off
591 cell, the two components capture a rapidly-adapting and a non-adapting components of the
592 response. **B:** Response spectra for individual stimuli (grey) and the computed NNMF
593 components (red and blue). Asterisk shows stimulation frequency. **C:** Scatterplot of
594 (normalized) component weights vs distance from the receptive field center. Gaussian fits
595 are shown as thick lines. Each point represents one stimulus (bar) presentation. **D:**
596 Receptive field maps for the two components. A surround component can be localized for
597 the M cell but not the P cell, and the spatial map for the K-on/off cell demonstrates spatially
598 co-extensive on+off input.

599

600 **Figure 4.** Summary statistics for visual cells in the LGN. **A:** Observed receptive field center
601 and surround strength. **B:** Ratio of surround gain to center gain vs. eccentricity, measured
602 with bars (large markers) and drifting grating stimuli (small markers). Box charts (right) show
603 the range, median, and intra-quartile range of gain ratio for the flashing-bar and drifting-
604 grating stimuli. **C:** Correlation between receptive field center radii (Eq. 3) measured with
605 drifting grating stimuli or flashing bars. **D:** Receptive field center and surround radius vs.
606 eccentricity, as measured using flashing bars and drifting gratings.

607

eNeuro Accepted Manuscript

608 **Figure 5.** Example mouse RGC responses. **A:** Representative traces for stimuli intersecting
609 the receptive field center. From top to bottom, an A2 ON cell, an A2 OFF cell, and a C6 cell.
610 Horizontal bar shows stimulus onset and duration. Timecourses of the first three NNMF
611 components (i, ii, iii) are shown separately for the C6 cell. **B:** Dendritic morphology of these
612 cells. Bottom panel shows spatial profiles for components (i, ii, iii) of the C6 cell. **C:**
613 Receptive field maps for these cells. Receptive field strength is given in imp/s per 100 × 100
614 μm^2; 1 pixel = 12 μm^2. Lower two panels show maps for components (i) and (iii) of the C6
615 cell. **D:** Relationship between dendritic field diameter and measured receptive field
616 diameter for our sample of mouse RGCs. Morphology of traced RGCs shown at 1/10 scale.
617
618 **Figure 6.** Example and summary statistics for correlation between physiology and anatomy.
619 **A:** Receptive field map for an A-on RGC, in imp/s per 100×100 µm. **B:** Contour plot of
620 receptive field showing outlines of 90% (red outline) and 50% (orange outline) of the peak
621 response relative to the cell dendritic morphology. **C:** Correlation between receptive field
622 strength and dendrite density, at 1 point per 12 μm^2, showing fitted relationship between
623 physiological and anatomical data. **D:** Summary r^2 values across the population of RGCs.
624 Arrowhead indicates cell shown in (A-C).
625
626
627
628

eNeuro Accepted Manuscript

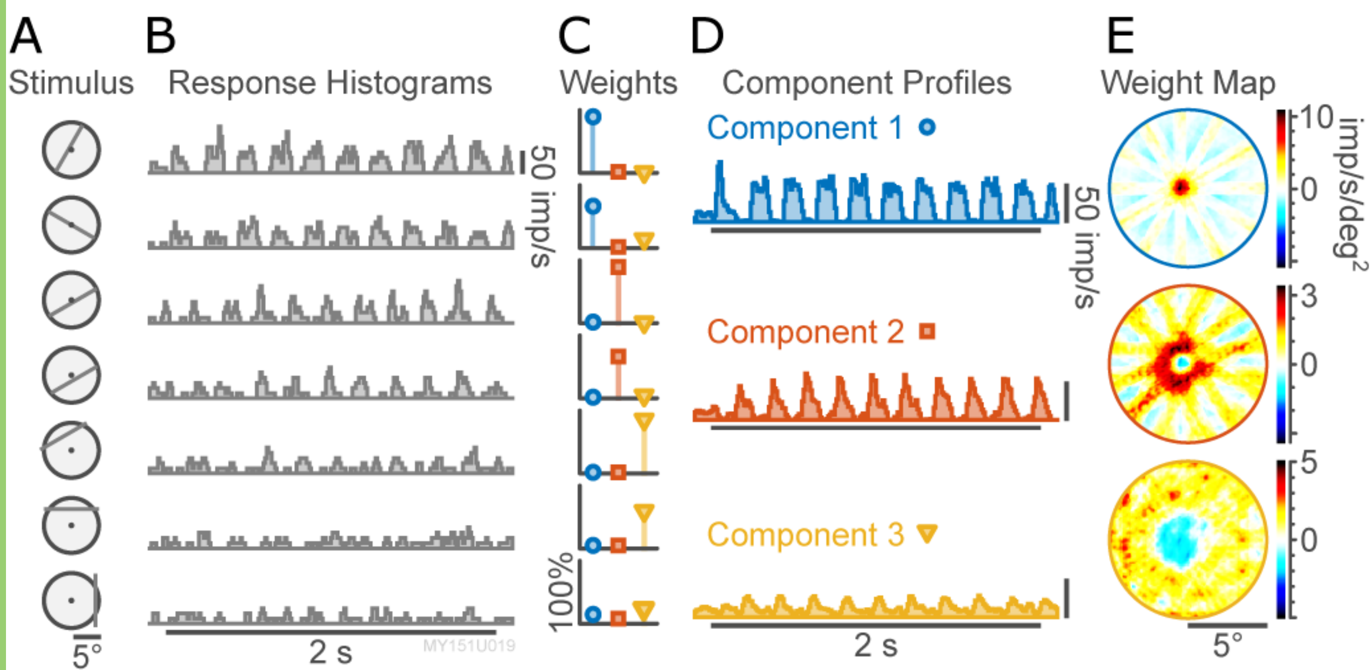

eNeuro Accepted Manuscript

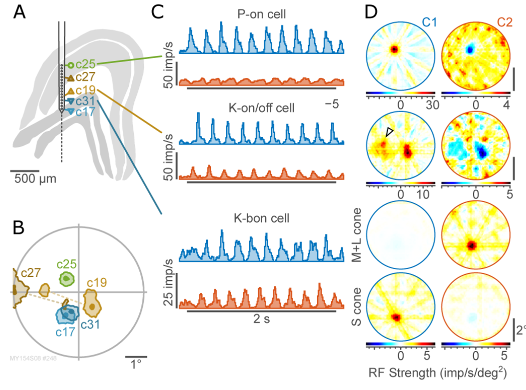

eNeuro Accepted Manuscript

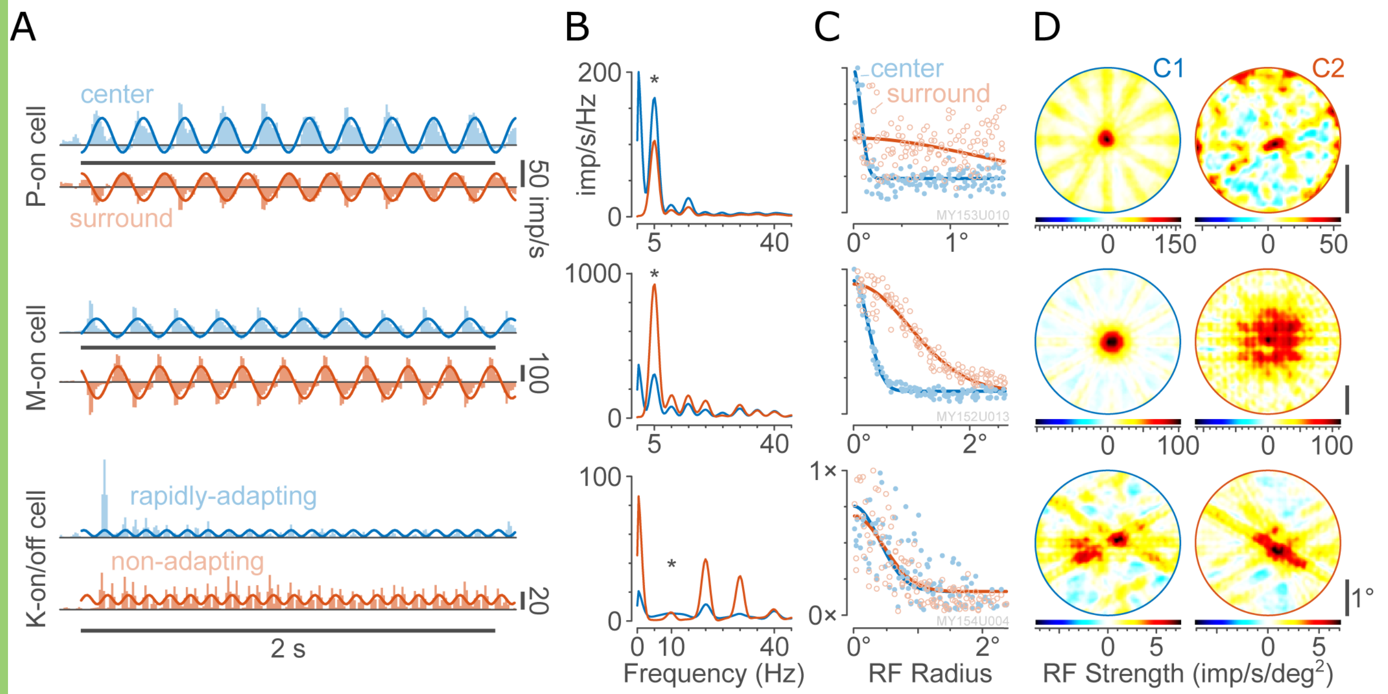

eNeuro Accepted Manuscript

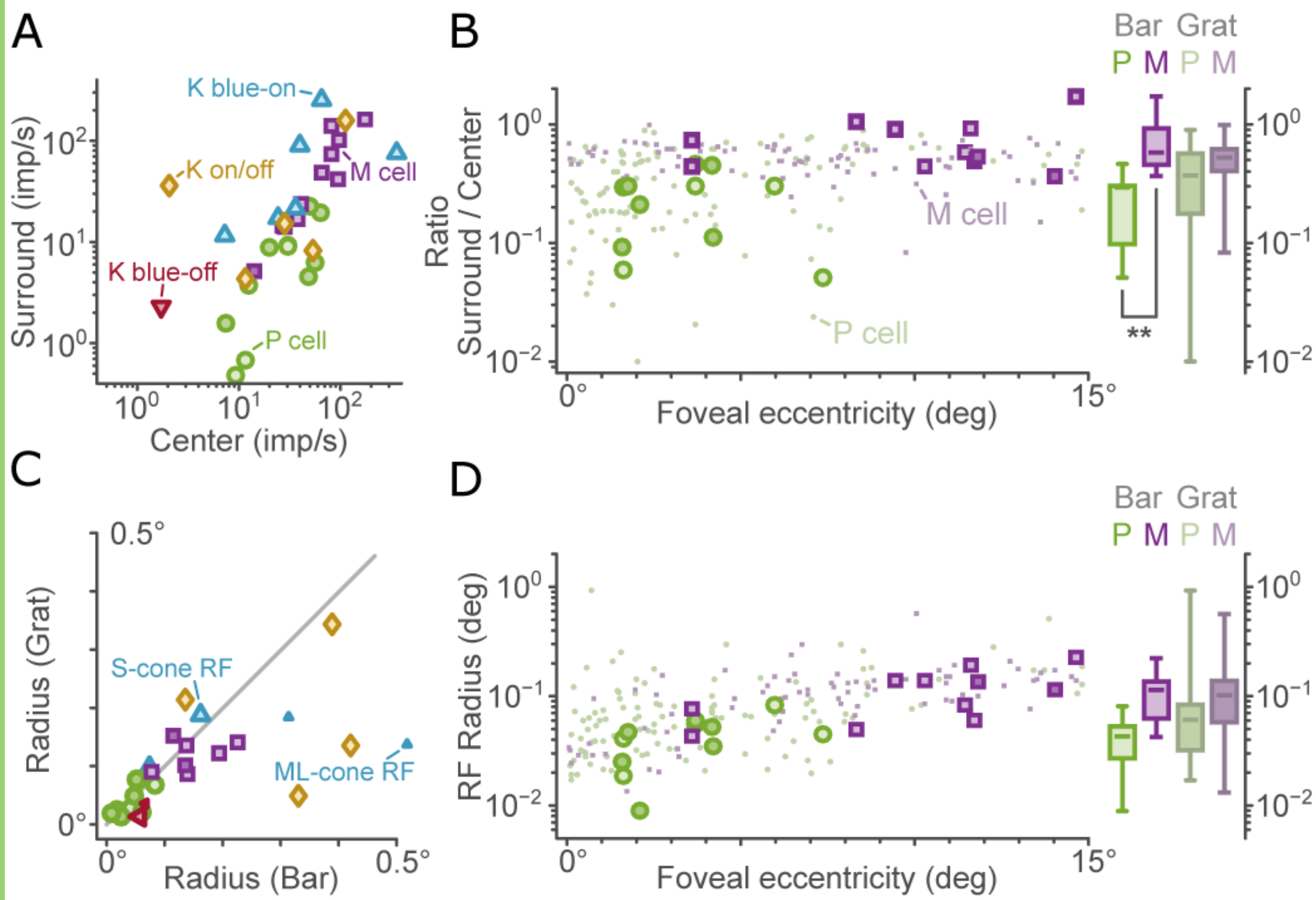

eNeuro Accepted Manuscript

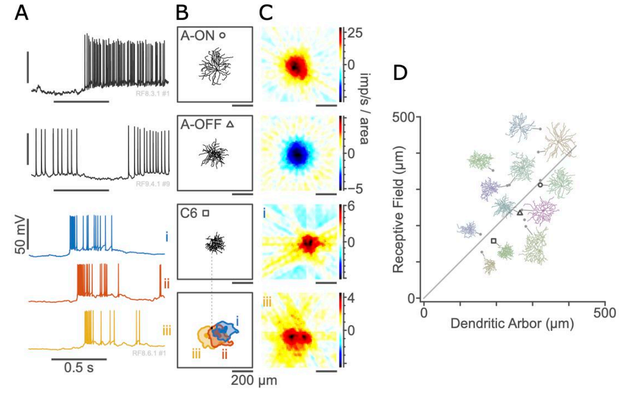

eNeuro Accepted Manuscript